Decaying Turbulence with Steady, Non-Uniform Background Density Stratification

By DAVID A. HEBERT
AND
STEPHEN M. DE BRUYN KOPS

Department of Mechanical and Industrial Engineering,

University of Massachusetts Amherst, Amherst, MA 01003

8 December 2011

Density stratification in geophysical flows can be non-uniform in the vertical direction, particularly in thermohaline staircases and atmospheric layer transitions. The description of flows in these regions, however, is often simplified to be in terms of the average ambient density change with height. This simplification is almost always made in numerical simulations because it greatly simplifies the calculations. In this paper high resolution direct numerical simulations of an idealized turbulent wake in a non-uniformly stratified fluid are analyzed to understand the consequences of assuming linear stratification. For flows with the same average change in density with height, but varied local stratification $d\overline{\rho}(z)/dz$, flow dynamics are dependent on the ratio $\xi = \delta_{\mathcal{U}}/\delta_{\rho}$, where $\delta_{\mathcal{U}}$ and δ_{ρ} are characteristic velocity and density vertical scale heights of the mean flow. Results suggest that a stably stratified flow will demonstrate characteristics similar to nonstratified flow when $\xi > 2$, even though the average stratification is quite strong. In particular, the results show that mixing is enhanced when $\xi > 2$, compared to linear stratification,

which may provide an explanation for under prediction of mixing by current planetary energy budget models.

---

1. Introduction

Geophysical flows can often be considered to have an ambient density that varies with height and to be invariant on the time scales of turbulent motion. Denoting by $\overline{\rho}(z)$ the time-independent ambient density at vertical position, z, we define the "stratification" as $d\overline{\rho}(z)/dz$. Our interest is in the stabilizing stratification that occurs in much of the ocean and atmosphere since understanding and modeling its effects on turbulence is important to predicting weather and climate and the related turbulent transport of heat, momentum and species. In particular, we focus on the dynamics of turbulence when the stratification is not uniform and on the modeling biases that may occur if a non-uniformly stratified flow is modeled as if it were uniformly stratified (i.e., as if $d\overline{\rho}(z)/dz$ were a constant).

Numerous investigations have been performed concerning flow in density stratified fluids. Laboratory studies include flows of turbulent wakes (e.g., Chomaz *et al.* 1993; Spedding *et al.* 1996; Spedding 2002; Bonnier & Eiff 2002), grid generated turbulence (e.g., Liu 1995; Fincham *et al.* 1996; Praud *et al.* 2005), and dynamics of monopoles and dipoles (e.g., Billant & Chomaz 2000*a*; Beckers *et al.* 2001, 2002). Also, several numerical studies have been performed to investigate how density-stratified fluids behave; examples include horizontal layer decoupling (Herring & Métais 1989; Métais & Herring 1989; Waite & Bartello 2004), turbulent mixing (Winters & D'Asaro 1996; Staquet 2000; Gargett *et al.* 2003; Peltier & Caulfield 2003), turbulence parameterization (Smyth & Moum 2000*b*; Shih *et al.* 2005; Hebert & de Bruyn Kops 2006*b*), and flow energetics (Ivey & Imberger 1991; Lindborg 2006).

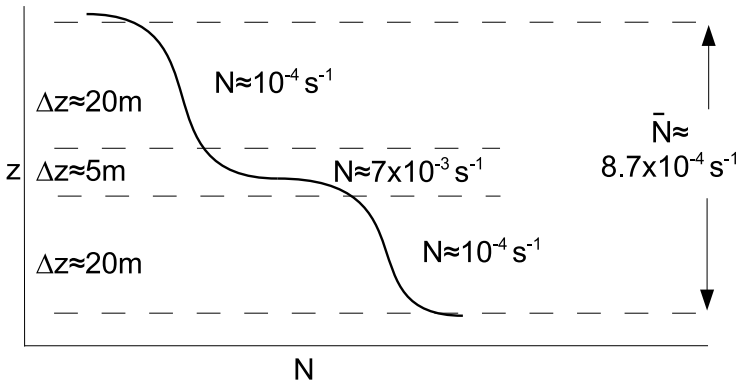

FIGURE 1. Cartoon of thermohaline staircase showing two layers subjected to moderate stratification separated by an interface of strongly stratified fluid (adapted from Gregg & Sanford (1987)). In the thermocline, the interface stratification can be 40-100 times larger than the layer stratification. Note the average density stratification $\Delta\overline{\rho}/\Delta z$ is significantly smaller than the interface stratification.

In the analysis of density-stratified flows, the assumption that the stratification is uniform and not a function of height is commonly made (e.g., Riley *et al.* 1981; Jacobitz *et al.* 1997; Billant & Chomaz 2000*b*; Riley & de Bruyn Kops 2003). However, in natural settings such as the atmosphere (Gossard *et al.* 1985; Dalaudier *et al.* 1994; Muschinski & Wode 1998) and the ocean (Williams 1974; Molcard & Tait 1977; Lambert & Sturges 1977; Schmitt *et al.* 1987; Boyd 1989), density layers or "staircases" can form in which areas of well-mixed fluid are separated by thin, high density-gradient layers. Assuming an average density stratification $\Delta\overline{\rho}/\Delta z = (\overline{\rho}_{top} - \overline{\rho}_{bottom})/(z_{top} - z_{bottom})$ in these regions will neglect the effect of local stratification differences (Figure 1).

Previous studies have been performed to investigate shear flow in which the initial vertical velocity and density profiles vary with height. For example, Smyth *et al.* (2005) investigate the ratio of turbulent diffusivities, Smyth *et al.* (2001) investigate the mixing efficiency, Γ, parameterized by the ratio of Ozmidov to Thorpe length scales, Smyth & Moum (2000*b*,*a*) investigate the length scales of turbulence in a shear flow, and D'Asaro

et al. (2004) investigate mixing estimates using Lagrangian tracers. In each of these studies the initial density (and velocity) profiles are a function of vertical position and change as the simulation evolves. An important difference between those studies and the current research is that here the ambient vertical density profile, $\overline{\rho}(z)$, (and hence the density stratification) is constant in time, thereby modeling a persistent, steady state thermohaline staircase or atmospheric transition layer.

The objective of this study is to investigate the effect of non-uniform density stratification on an idealized late wake. In particular, the wake has no mean shear, hence the flow is decaying. The wake has zero mean velocity, similar to that generated by a self-propelled object (although Meunier & Spedding (2006) note that it is very difficult to obtain a truly momentumless wake in a stratified fluid). The behavior of the simulated flow is investigated for a range of stratification profiles superimposed on the same initial velocity field. The methodology and simulations are described in §2 followed by a detailed discussion of the dynamics of the simulated flow in §3. In particular, the concept of available potential energy in the context of this flow is developed in §3.2.2. Modeling implications and conclusions are presented in §4.

2. Methodology

2.1. *Simulation Overview*

High resolution direct numerical simulations (DNS's) of a perturbed von Kármán vortex street are conducted. The initial conditions consist of three vortex pairs and low-level noise. There is no ambient shear and the the ambient stratification is a function of height and held constant in time. Each vortex is initialized with the following velocity profile

(c.f. de Bruyn Kops *et al.* 2003):

$$\widetilde{\mathbf{V}}_\theta = \widetilde{\mathcal{U}} \frac{\tilde{r}}{\tilde{r}_m} \exp\left[\frac{1}{2}\left(1 - \left(\frac{\tilde{r}}{\tilde{r}_m}\right)^2\right)\right] \mathrm{sech}^2\left(\frac{\tilde{z}}{\tilde{\delta}_\mathcal{U}}\right) \ , \tag{2.1}$$

where $\widetilde{\mathcal{U}}$ is the initial velocity scale, $\tilde{r}_m$ is a radial length scale, $\tilde{\delta}_\mathcal{U}$ is the velocity scale height, $\tilde{r} = \sqrt{\tilde{x}^2 + \tilde{y}^2}$ is the radial position, and $\tilde{z}$ is the vertical position. Note the convention of denoting dimensional quantities by $(\tilde{\cdot})$ will be followed throughout this paper. The separation distances between vortex centers in the $\tilde{x}$ and $\tilde{y}$ directions are $\tilde{s}_x = 2\tilde{r}_m$ and $\tilde{s}_y = 1.5\tilde{r}_m$. In creating the initial flow condition noise is applied to $\tilde{r}_m$, $\tilde{\delta}_\mathcal{U}$, $\tilde{s}_x$, $\tilde{s}_y$; each is randomly perturbed up to 5% of its nominal value. For example, the vertical scale for each vortex is calculated as $\tilde{\delta}_\mathcal{U} + 0.05\lambda\tilde{\delta}_\mathcal{U}$, and the y positions for the positive vortices are calculated as $\tilde{L}_y/2 + \tilde{s}_y/2 + 0.05\lambda\tilde{s}_y$, where λ is a [-1 1] uniformly distributed random number and $\tilde{L}_y$ is the span-wise (y) domain width.

The ambient density, $\tilde{\overline{\rho}}(\tilde{z})$, is imposed with a hyperbolic tangent vertical profile,

$$\tilde{\overline{\rho}}(\tilde{z}) = \frac{\Delta\tilde{\overline{\rho}}}{2}\tanh\left(\frac{-\tilde{z}}{\tilde{\delta}_\rho}\right) \ , \tag{2.2}$$

from which the density stratification, $d\tilde{\overline{\rho}}(\tilde{z})/d\tilde{z}$, is obtained:

$$\frac{d\tilde{\overline{\rho}}(\tilde{z})}{d\tilde{z}} = -\frac{1}{2}\frac{\Delta\tilde{\overline{\rho}}}{\tilde{\delta}_\rho}\mathrm{sech}^2\left(\frac{-\tilde{z}}{\tilde{\delta}_\rho}\right) . \tag{2.3}$$

Here $\Delta\tilde{\overline{\rho}} = \tilde{\overline{\rho}}_{top} - \tilde{\overline{\rho}}_{bottom}$ is the difference in density between the top and bottom of the numerical domain, $\tilde{z}$ is the vertical position, and $\tilde{\delta}_\rho$ is a characteristic height of the density profile. The vertical profiles of both the velocity (2.1) and density stratification (2.3) are sech^2, with each having a different scale height, $\tilde{\delta}_\mathcal{U}$ and $\tilde{\delta}_\rho$. The parameter ξ is now defined which describes the ratio of the momentum vertical length scale, $\tilde{\delta}_\mathcal{U}$, to the stratification vertical length scale, $\tilde{\delta}_\rho$, (shown graphically in Figure 2):

$$\xi \equiv \frac{\tilde{\delta}_\mathcal{U}}{\tilde{\delta}_\rho}. \tag{2.4}$$

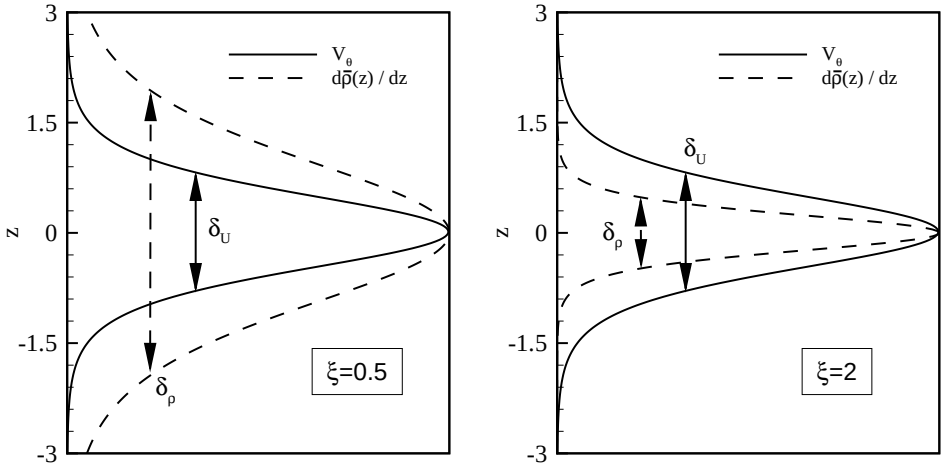

FIGURE 2. Velocity profile (solid) and density stratification (dashed) for (left) $\xi = 0.5$ and (right) $\xi = 2$.

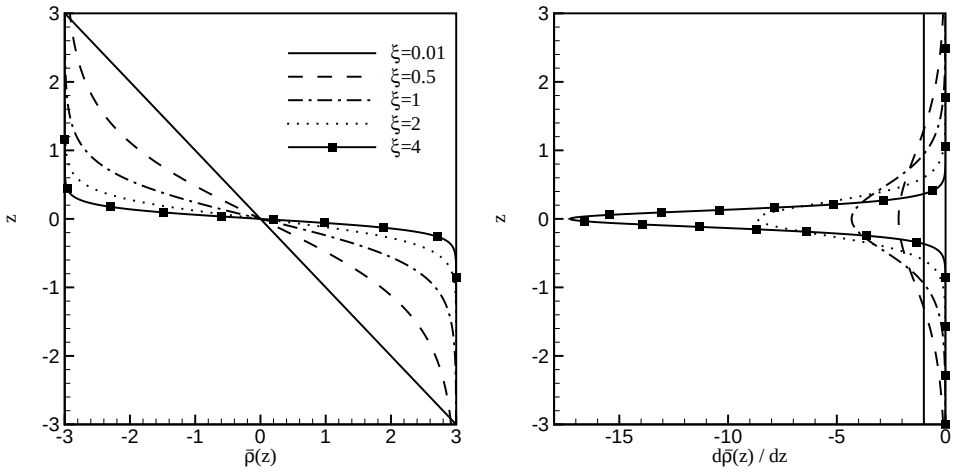

FIGURE 3. Ambient (nondimensional) density profile (left) and stratification profile (right) for several different ξ (see (2.4)). Note $\Delta\overline{\rho}/\Delta z = -1$ for each ξ, but locally $d\overline{\rho}(z)/dz$ is different.

The velocity scale height is the same in all simulations; only $\tilde{\delta}_\rho$ is varied to obtain different values of ξ. The vertical profiles of $\overline{\rho}(z)$ and $d\overline{\rho}(z)/dz$ for each ξ are shown in Figure 3. Note that while locally $d\overline{\rho}(z)/dz$ differs for each ξ, the average change in density with height is the same (i.e., $\Delta\overline{\rho}/\Delta z = -1$).

It is evident from the right plot of Figure 3 that there is a region or "layer" of very

strong density stratification in the center of the domain. Here the density stratification layer is defined as the region where $|d\overline{\rho}(z)/d(z)| > 0.1$, and is chosen as 10% of the stratification value when the flow is nearly linearly stratified, that is when $\xi = 0.01$.

2.2. *Governing Equations*

The flow fields are assumed to satisfy the Navier-Stokes equations subject to the Boussinesq approximation. (A nice summary of the Boussinesq approximation is provided by Spiegel & Veronis (1960)). Taking $\widetilde{\mathcal{U}}$ as the velocity scale, $\tilde{r}_m$ as the length scale, $\tilde{r}_m|\Delta\tilde{\overline{\rho}}/\Delta\tilde{z}|$ as the density scale (where $|\cdot|$ denotes absolute value), $\tilde{r}_m/\widetilde{\mathcal{U}}$ as a time scale, and $\tilde{\rho}_0\widetilde{\mathcal{U}}^2$ as a pressure scale (where $\tilde{\rho}_0$ is the reference density value), the nondimensional governing equations in a non-rotating frame of reference are:

$$\nabla \cdot \mathbf{v} = 0 \tag{2.5a}$$

$$\frac{\partial \mathbf{v}}{\partial t} + \mathbf{v}\cdot\nabla\mathbf{v} = -\left(\frac{2\pi}{\overline{\mathrm{F}}_r}\right)^2 \rho\mathbf{e}_z - \nabla p + \frac{1}{\mathrm{Re_r}}\nabla^2\mathbf{v} \tag{2.5b}$$

$$\frac{\partial \rho}{\partial t} + \mathbf{v}\cdot\nabla\rho + w\frac{d\overline{\rho}(z)}{dz} = \frac{1}{\mathrm{Re_r Sc}}\nabla^2\rho \tag{2.5c}$$

where $\mathbf{v} = (u, v, w)$ is the velocity vector, ρ and p are the density and pressure deviations from their ambient values, and $\mathbf{e}_z$ is a unit vector in the vertical direction. The Reynolds, Froude, and Schmidt numbers are defined as:

$$\mathrm{Re_r} = \frac{\widetilde{\mathcal{U}}\tilde{r}_m}{\tilde{\nu}} \qquad\qquad \overline{\mathrm{F}}_r = \frac{2\pi\widetilde{\mathcal{U}}}{\widetilde{\overline{\mathrm{N}}}\tilde{r}_m} \qquad\qquad \mathrm{Sc} = \frac{\tilde{\nu}}{\widetilde{\mathcal{D}}}, \tag{2.6}$$

where $\widetilde{\overline{\mathrm{N}}}^2 = -\tilde{g}/\tilde{\rho}_0(\Delta\tilde{\overline{\rho}}/\Delta\tilde{z})$ is the average buoyancy (or Brunt-Väisälä) frequency, and $\widetilde{\mathcal{D}}$ is an "effective" mass diffusivity that represents the effects of salt diffusivity (ocean) or water vapor diffusivity (atmosphere) and thermal diffusivity.

All simulations are conducted using a pseudo-spectral technique by which spatial derivatives are computed using spectral methods. Time advancement is performed using a third-order Adams-Bashforth scheme with pressure projection. A spherical wave-number

truncation of approximately 15/16 κ_{max}, with κ_{max} the maximum wave number in the discrete Fourier transforms, is used to eliminate the most damaging aliasing errors. The momentum equation is advanced in time with the nonlinear term computed in vorticity form. As suggested by Kerr (1985), an alternating time-step scheme is employed for the density field to approximate the skew-symmetric form of the non-linear term, thereby minimizing aliasing errors (Boyd 2001).

Periodic boundary conditions are imposed in all directions for the simulations. This can be achieved because the stratification is periodic in the vertical direction ($\mathrm{sech}^2(z)$). Since the governing equations include density stratification $d\tilde{\overline{\rho}}(\tilde{z})/d\tilde{z}$, and not $\tilde{\overline{\rho}}(\tilde{z})$, periodic boundary conditions for this particular flow can be used.

All numerical simulations are conducted with $\overline{\mathrm{F}}_r = 2.75$ and $\mathrm{Re_r} = 19200$. In addition, Sc is set to 1, close to the ratio of momentum to heat diffusivity in air but far from the Schmidt number for salt in water. The nondimensional computational domain size for each simulation is $L_x = 12$ and $L_y = L_z = 6$, while the number of gridpoints in each direction is $N_x = 1024$, $N_y = N_z = 512$. This results in grid spacing Δx=0.0117. We can estimate the spatial resolution by noting that with $\varepsilon \approx 0.0035$ (from Figure 14(a)) the Kolmogorov length scale $\mathrm{L_K} \equiv (\nu^3/\varepsilon)^{1/4} \approx 0.0026$. This is about 5 times smaller than Δx and consistent with good resolution for DNS (Moin & Mahesh 1998). Kolmogorov's 1962 refined similarity theory (Kolmogorov 1962) is recalled, however, which suggests that local, intermittent turbulence can be expected at scales much smaller than is typically resolved in a DNS, even in unstratified flows.

The only difference between the initial conditions of each simulation is the stratification profile; δ_ρ is chosen so that $0.01 \leq \xi \leq 4$. In other words, the velocity vertical scale ranges from 100 times smaller to 4 times greater than the density vertical length scale (see Figure 3). Values of δ_ρ and $\delta_{\mathcal{U}}$ for each simulation are summarized in Table 1. The case

ξ	0.01	0.5	1	2	4	NoStrat
δ_ρ	69.4	1.39	0.694	0.347	0.174	N/A
$\delta_\mathcal{U}$	0.694	0.694	0.694	0.694	0.694	0.694

TABLE 1. Conditions for simulated flows

of $\xi = 0.01$ is so close to being linearly stratified over the range of z in the simulations that a separate linearly stratified case is not considered. The unstratified case is also considered for comparison since, when $\xi \gg 1$, much of the flow is subjected to very mild stratification.

3. Simulation Results

3.1. *General Flow Features*

Insight into the general flow dynamics can be obtained via use of the horizontal stream function, ψ (Riley & Lelong 2000):

$$\widehat{\mathbf{v}} = i(\mathbf{e}_z \times \kappa)\widehat{\psi},$$

where κ is the three dimensional wavenumber and $\widehat{(\cdot)}$ denotes Fourier transformed quantity. A time-series plot of the center ψ is shown in Figure 4 for the case with ξ=0.01. Cases having other ξ values demonstrate qualitatively similar results. At t=0 the von Kármán vortex street is clear with light colors representing positive vortices and dark colors representing negative vortices. As the simulated flow advances in time the vortices interact with each other and vortex pairing occurs by $t = 15$.

As the flow evolves vertical velocity w can be generated by internal waves and instabilities including shear (e.g., Holmboe 1962; Lilly 1983; Riley & de Bruyn Kops 2003) and "zig-zag" (Billant & Chomaz 2000c,a) instabilities. Since the flow was initialized

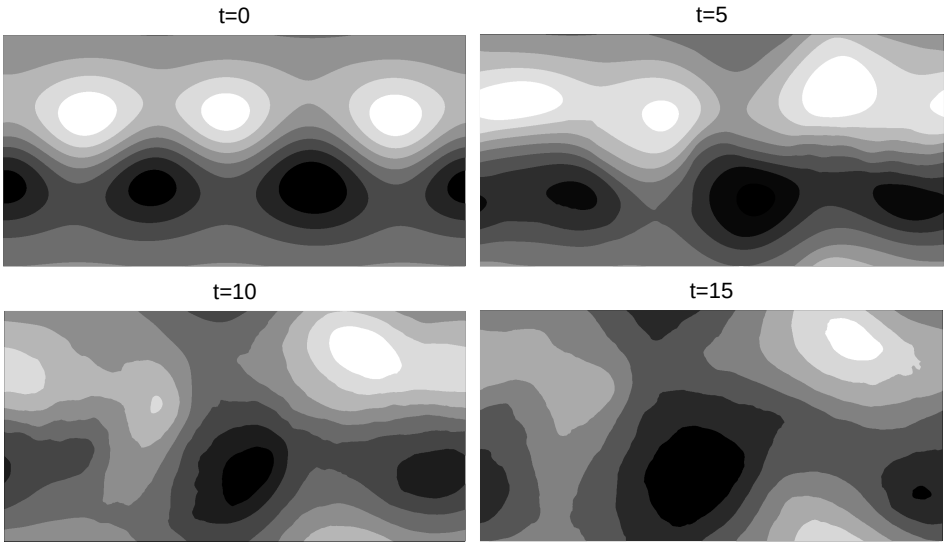

FIGURE 4. Contour plot of center plane stream function ψ for ξ=0.01. Light colors represent positive values of ψ, dark colors represent negative values.

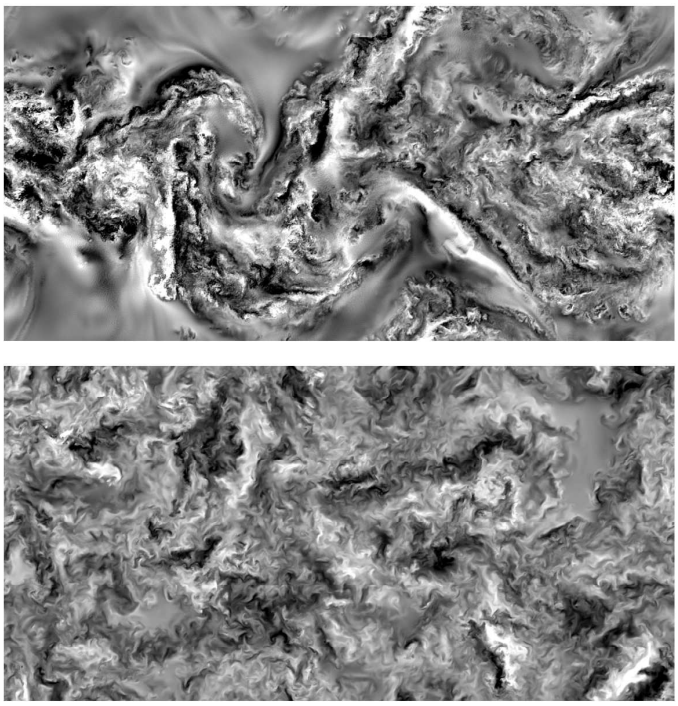

FIGURE 5. Center plane ($z = 0$) vertical velocity for $\xi = 0.01$ (upper plot) and no stratification (lower plot). Dark colors represent negative (downward) velocity, light colors represent positive velocity.

with $w = 0$, it can be used as an indicator of regions of turbulence generation. Figure 5 contains plots of vertical velocity for $\xi = 0.01$ (upper plot) and no stratification (lower plot) at $t = 10$. For the stratified flows intermittent turbulent patches form, consistent with prior studies regarding density stratified flows, which suggests the simulations are representative of flows observed in laboratory and natural settings. Also, since vertical motion is shown to be related to the Richardson number below, it is shear instabilities that are believed to be causing vetical motions. (Further instability discussion can be found in §4).

3.1.1. *Shear and Richardson Number*

In stratified flows dominated by vortical modes, such as those simulated in this study, it is postulated that horizontal layer decoupling occurs and that the flow will be susceptible to Kelvin-Helmholtz shear instabilities (Lilly 1983). The square of the vertical shear of horizontal motions is defined as:

$$S^2 = \left(\frac{\partial u}{\partial z}\right)^2 + \left(\frac{\partial v}{\partial z}\right)^2 . \tag{3.1}$$

Figure 6 contains plots of the horizontally averaged square of vertical shear $\left\langle S^2 \right\rangle_H$ versus vertical position for several ξ and the non-stratified simulation, where $\langle \cdot \rangle_H$ denotes averaging over xy-planes. Initially, the shear profile demonstrates a "bimodal" pattern, with maximum values at $z \pm 0.5$, and is a result of the initial $\mathrm{sech}^2(z)$ velocity profile. For all the stratified cases the bimodal maximum shear pattern persists in time, but the peaks do not remain aligned with the peaks in the initial shear profile. Instead, the distance between peaks decreases in time (Figure 7(a)) as the peaks move toward the planes of maximum energy. This shift in the location of the maximum shear from that of the maximum shear in the initial conditions toward that of the maximum energy in the initial conditions is consisted with the results of Riley & de Bruyn Kops (2003), and suggests

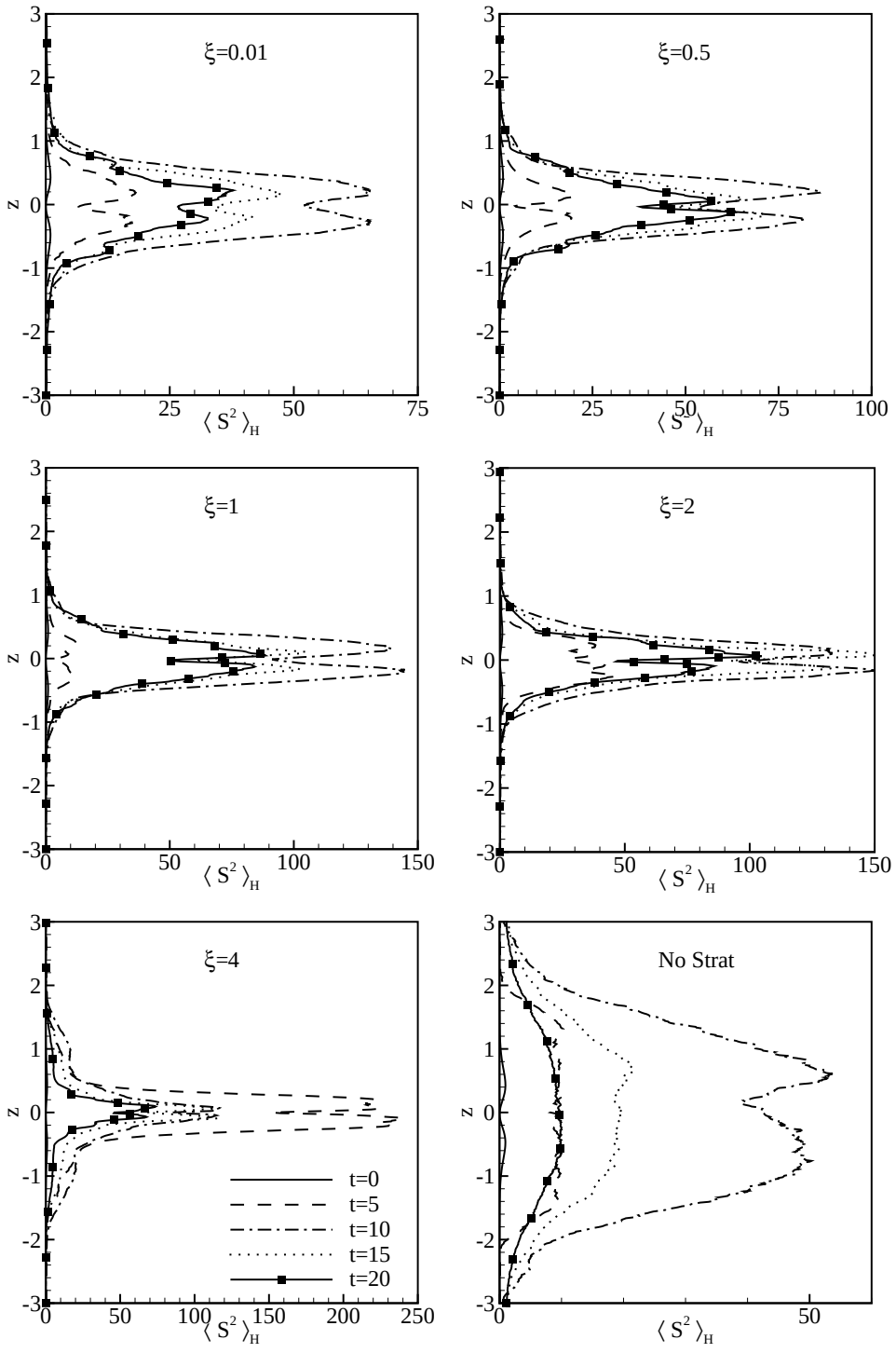

FIGURE 6. Time evolution of $\langle S^2 \rangle_H$ for several ξ and for the unstratified simulation. Note the difference in horizontal scale for each plot.

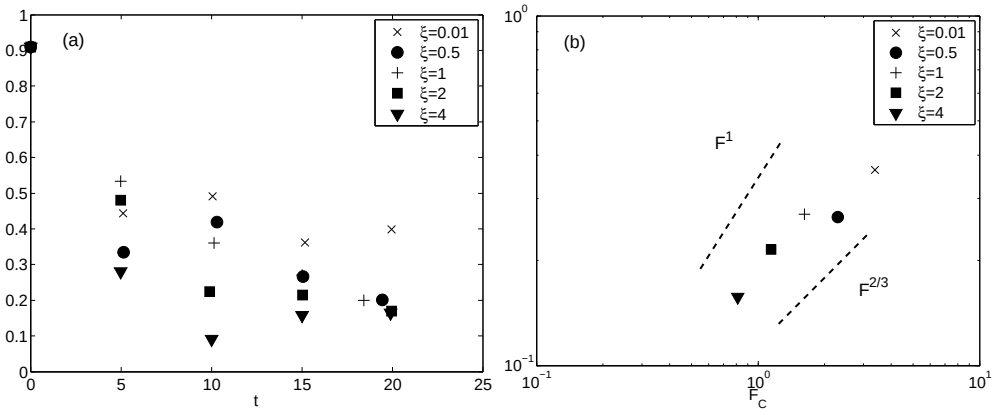

FIGURE 7. (a) Time evolution of peak $\langle S^2 \rangle_H$ vertical spacing. (b) Vertical spacing of $\langle S^2 \rangle_H$ versus F_C at $t = 15$.

that the peak shear is due to decouping of the horizontal motions as suggested by Lilly (1983) and not just from the initial conditions. In addition, the distance between the peaks in $\langle S^2 \rangle_H$ narrows with increasing ξ, which suggests a dependence of $\langle S^2 \rangle_H$ peak spacing on the centerline Froude number, $\mathrm{F}_C = 2\pi\widetilde{\mathcal{U}}/(\widetilde{\mathrm{N}}_C \tilde{r}_m)$, where $\widetilde{\mathrm{N}}_C$ is the centerline buoyancy frequency. Figure 7(b) contains a plot of vertical shear peak spacing versus F_C at $t = 15$, where indeed a dependence on F_C is evident. The decrease in $\langle S^2 \rangle_H$ with F_C is in agreement with vertical scaling arguments of Riley *et al.* (1981), Lilly (1983), and Billant & Chomaz (2001) in which the vertical scale of horizontal "pancake" eddies scales as $\widetilde{\mathcal{U}}/\widetilde{\mathrm{N}}_C$. In contrast, the bimodal pattern disappears by $t = 5$ for the non-stratified case in which horizontal decoupling does not occur.

It is interesting to note that the maximum $\langle S^2 \rangle_H$ increases as ξ is increased. This is due to the increase in local density stratification (Figure 3), which in turn causes stronger horizontal layer decoupling and an increase in the vertical shear between layers. Also, for $\xi = 4$, the maximum $\langle S^2 \rangle_H$ occurs much earlier in time than the other simulations. This can be explained by noting that when $\xi = 4$ a significant amount of $\langle S^2 \rangle_H$ occurs where there is no density stratification ($|z| > 0.75$), which results in the creation of

vertical overturning in this area (see Figure 12 below). The density stratification then acts as a boundary between the vertical overturning flow outside the stratification and the horizontal flow inside, and so more shear occurs.

A quantity related to vertical shear of horizontal motions is the gradient Richardson number, Ri, defined as the ratio of buoyancy to shear forces. The volume and planar averaged Ri are defined here as:

$$\langle \mathrm{Ri} \rangle = \left(\frac{2\pi}{\overline{\mathrm{F}}_r} \right)^2 \frac{1}{\langle S^2 \rangle} \tag{3.2}$$

$$\langle \mathrm{Ri} \rangle_H = \left(\frac{2\pi}{\overline{\mathrm{F}}_r} \right)^2 \frac{d\overline{\rho}(z)/dz}{\langle S^2 \rangle_H}, \tag{3.3}$$

where $\langle \cdot \rangle$ denotes volume averaged quantity. $\langle \mathrm{Ri} \rangle$ is shown in Figure 8(a). Initially $\langle \mathrm{Ri} \rangle$ is large, which indicates that there is insufficient shear to cause flow instabilities and turbulence. As the flow progresses in time, vertical decoupling of the horizontal motions occurs and $\langle \mathrm{Ri} \rangle$ rapidly decreases. The average Richardson number decreases to about 0.25, which supports the notion that Kelvin-Helmholtz instabilities are a mechanism by which turbulence occurs. Further discussion of instability mechanisms is in §4.

From Figure 8 it is apparent that the evolution of $\langle \mathrm{Ri} \rangle$ and the profiles of $\langle \mathrm{Ri} \rangle_H$ depend strongly on ξ. When $\xi \leq 1$ all but the tails of the wake are in the stratification layer and the flows behave as expected based on similar simulations of uniformly stratified turbulence. In particular, the development of the flow is qualitatively independent of the strength of the stratification in the core of the wake, but the time for decoupling of the horizontal motions to occur and $\langle \mathrm{Ri} \rangle$ to reach its minimum value increases slightly with increased stratification. When $\xi > 1$, however, the wake profile is wider than the stratification layer and the regions initialized with the highest shear are not strongly constrained in the vertical direction by buoyancy forces.

For the simulations with $\xi \leq 1$ the minimum $\langle \mathrm{Ri} \rangle_H$ is located near $z = 0$ since the

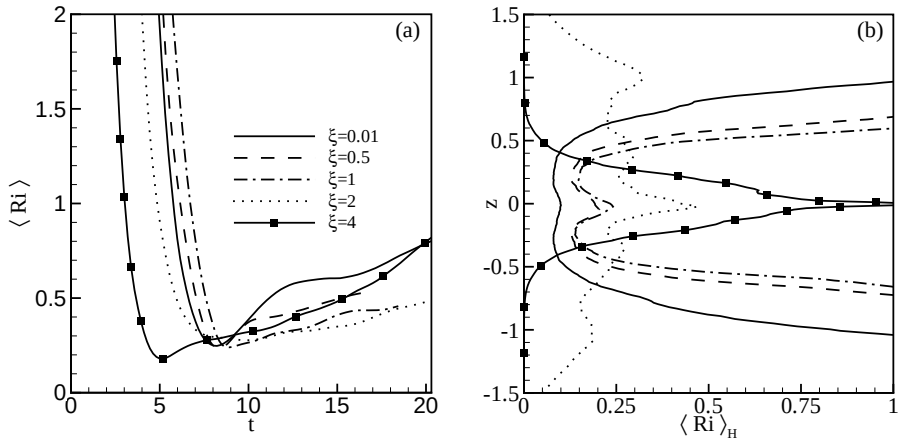

FIGURE 8. (a) $\langle \mathrm{Ri} \rangle$ versus time, (b) Vertical profile of $\langle \mathrm{Ri} \rangle_H$ versus height at $t = 10$. Note that all simulations begin with $\langle \mathrm{Ri} \rangle = 25$. Also note the profiles of Ri with $\xi \geq 2$ are fundamentally different from those with $\xi < 2$.

entire wake is inside the density stratification layer. In contrast, when $\xi > 1$, some of the wake is outside the stratification layer and the minimum $\langle \mathrm{Ri} \rangle_H$ occurs at $|z| > 1.5$. This behavior of Ri helps explain the large vertical kinetic energy shown in Figure 12 below, particularly for $\xi = 4$.

3.1.2. *Horizontal Length Scale*

Flows subject to stable density stratification often demonstrate a horizontal length scale that increases in time. This quality is evident in the evolution of the horizontal streamfunction on the center plane (Figure 4). Theoretical arguments suggest that a horizontal length based on an advective time scale, $\ell_H \sim u_H^3/\varepsilon$, can be calculated. However, in flows that demonstrate intermittent turbulence, use of such an advective length scale can result in unrealistic values of ℓ_H (Hebert & de Bruyn Kops 2006*a*). Instead, a horizontal length scale is defined based on the cross-correlation of velocity:

$$R_{yx}(r) = \frac{\langle v(x+r)v(x) \rangle_H}{\langle v^2 \rangle_H}\,, \tag{3.4}$$

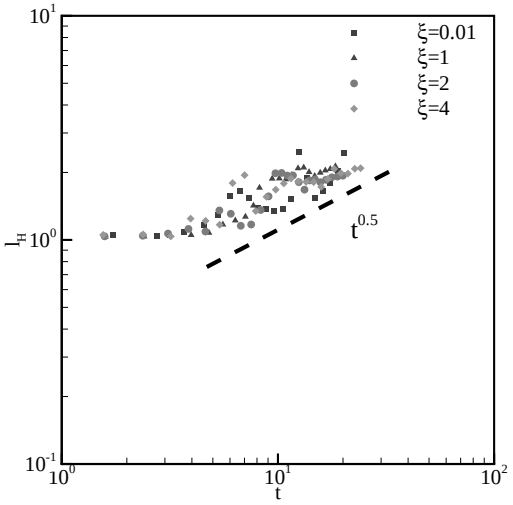

FIGURE 9. ℓ_H for several stratified simulations.

where the R_{yx} denotes the correlation of y direction velocity (v) in the x direction. The horizontal length scale is then defined as the distance r when $R_{yx} = 0$:

$$\ell_H = r, \quad \text{where } R_{yx}(r) = 0 \ . \tag{3.5}$$

Figure 9 contains a plot of ℓ_H for all ξ. After $t = 5$, when the response to the flow initial condition has subsided, the length scale increases in time and is proportional (although somewhat noisy) to $t^{0.5}$. This result is in agreement with the integral length scale results of Praud *et al.* (2005), who also found a slightly variable time evolution of ℓ_H but an overall trend of $t^{0.5}$.

3.2. *Flow Energetics*

3.2.1. *Kinetic Energy*

The horizontal and vertical contributions to kinetic energy are defined as:

$$E_H = \frac{1}{2}\left(u^2 + v^2\right) \quad E_V = \frac{1}{2}\left(w^2\right) \tag{3.6}$$

A general idea of the flow energetics can be seen by examining the x-direction spectrum of horizontal energy, $\widehat{E}_h(k_x)$, defined as:

$$\widehat{E}_H(k_x) = \frac{1}{2}\left(\widehat{u}(k_x)\widehat{u}(k_x)^* + \widehat{v}(k_x)\widehat{v}(k_x)^*\right) .$$

Here $\widehat{u}(k_x)$ and $\widehat{v}(k_x)$ are the x and y components of velocity Fourier transformed in the x-direction, $(\cdot)^*$ denotes complex conjugate, and k_x denotes x-direction wave number. $\widehat{E}_H(k_x)$ is obtained by summing over each k_x for the entire domain rather. Thus, $\widehat{E}_H(k_x)$ is the energy spectra of the entire domain, not just for a single horizontal plane of motion. Figure 10(a) contains a plot of the time evolution of $\widehat{E}_H(k_x)$ for $\xi = 1$, which is representative of the spectrum of all simulations conducted in this study. The initial peak at $k_x \approx \pi/2$ corresponds to the separation distance between vortices. As the flow evolves, transfer of energy to smaller scales is observed as the magnitude of $\widehat{E}_H(k_x)$ at larger wave numbers increases between $t = 0$ and $t = 10$. After $t = 10$ the energy at all wave numbers decreases as the flow decays. In addition, once the flow has had time to develop from the initial conditions ($t > 10$), it displays a near $k_x^{-5/3}$ spectrum. This $k_x^{-5/3}$ dependence is seen for all ξ (Figure 10(b)), and is in agreement with the results of Lindborg (2006).

The time evolution of the volume averaged $\langle E_H \rangle = 0.5\left\langle u^2 + v^2 \right\rangle$ and $\langle E_V \rangle = 0.5\left\langle w^2 \right\rangle$ for each ξ is shown in Figures 11(a), (b). As ξ is increased from 0.01 to 2, the trend is for $\langle E_H \rangle$ to persist longer in time and the magnitude of $\langle E_V \rangle$ to decrease, compared with the unstratified flow. These trends are expected since the vortex "core" is more strongly stratified, which leads to greater horizontal motion decoupling and less vertical motion. However, these trends are reversed when $\xi > 2$, and the flow demonstrates traits similar to non-stratified flow. This is because the characteristic height of the wake is much smaller than the density stratification height, which results in a significant portion of the wake being subjected to very weak density stratification. It is interesting that the transition

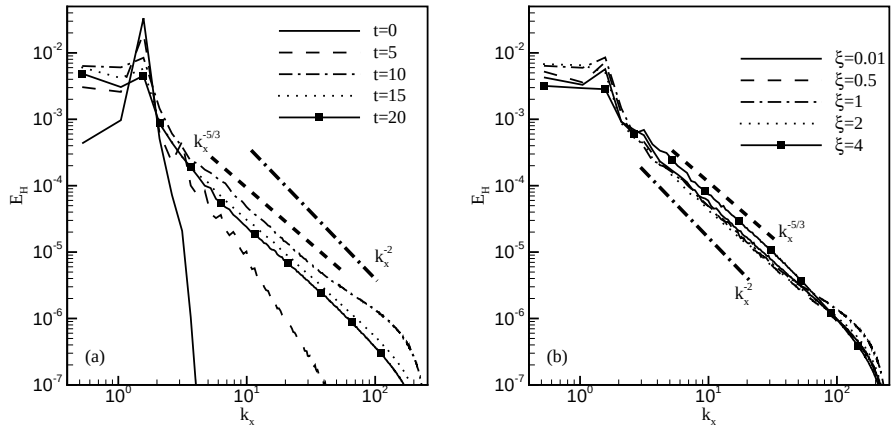

FIGURE 10. (a) Evolution of E_H x spectrum for $\xi = 1$; (b) E_H x spectrum for all ξ, $t = 10$. Note the heavy dashed line representing $k_x^{-5/3}$ and the dashed-dot line representing k_x^{-2}

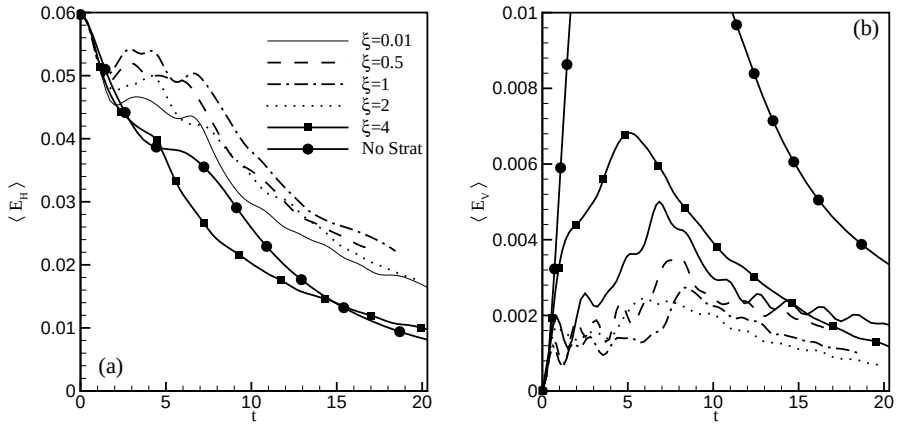

FIGURE 11. Time evolution of (a) $\langle E_H \rangle$; (b)$\langle E_V \rangle$.

occurs when $\xi > 2$, rather than $\xi > 1$. This suggests that it is the energy profile, and not the velocity profile, that determines when the flow will begin to demonstrate unstratified flow traits (see further discussion in §sec:conclusions). Thus, for the simulations with $\xi \leq 2$ the stratification acts as a boundary to confine $\langle E_V \rangle_H$. In contrast, when $\xi = 4$ a significant amount of $\langle E_V \rangle_H$ forms in regions outside the density stratification layer where there is no buoyancy force and overturning can readily occur. This can be seen in Figure 12, where $\langle E_V \rangle_H$ is plotted versus z for $\xi = 2$ and 4.

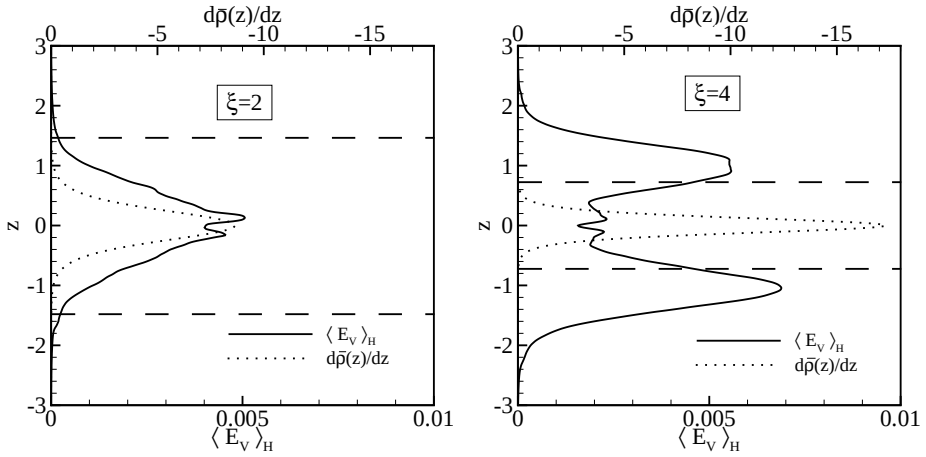

FIGURE 12. $\langle E_V \rangle_H$ at $t = 10$ for (left) $\xi = 2$ and (right) $\xi = 4$. Note upper horizontal axis corresponds to $d\bar{\rho}(z)/dz$, and lower horizontal axis corresponds to $\langle E_V \rangle_H$. The dashed lines mark where the stratification $|d\bar{\rho}(z)/dz| = 0.1$. When $\xi = 4$, a significant amount of vertical kinetic energy occurs outside the density stratification.

3.2.2. *Available Potential Energy for Non-uniform Density Stratification*

Discussion of potential energy usually involves the concepts of available and background potential energy, first suggested by Lorenz (1955). He noted that in order to convert the total potential energy in the Earth's atmosphere to kinetic energy, the temperature would need to be reduced to absolute zero and all mass would need to be located at sea level, conditions that cannot readily occur. (It is estimated that potential energy makes up 25% of the total energy (internal + potential + kinetic) in the Earth's atmosphere, while only 2% is kinetic energy (Gill 1982, pg.81)). Instead, the potential energy that is available for conversion to kinetic energy, $\widetilde{E}_p$, is said to be the result of any deviation from a background (or rest) potential energy, $\widetilde{E}_b$. $\widetilde{E}_b$ is a state that would exist if the fluid were adiabatically redistributed to a minimum energy state. The available potential energy is the total potential energy, $\widetilde{\mathcal{P}}$, minus the background potential energy:

$$\widetilde{E}_p = \widetilde{\mathcal{P}} - \widetilde{E}_b \,. \tag{3.7}$$

Initially, this might seem like a straightforward method for obtaining the available potential energy in a system. However, while $\widetilde{\mathcal{P}}$ is typically defined as $\iiint \tilde{\rho}_t \tilde{g} \tilde{z}\, d\tilde{x}\, d\tilde{y}\, d\tilde{z}$, where $\tilde{\rho}_t = \tilde{\rho}_0 + \tilde{\overline{\rho}}(z) + \tilde{\rho}$ is the total density equal to the sum of reference, ambient, and fluctuating components, several methods exist for obtaining $\widetilde{E}_b$. In a method described by Winters *et al.* (1995) and Staquet (2000), adiabatic redistribution is performed by sorting the density field so that the highest density parcels are in the lowest vertical position. The redistributed density field, $\tilde{\rho}_t^*$, is then used to calculate the background potential energy, $\widetilde{E}_b = \iiint \tilde{\rho}_t^* \tilde{g} \tilde{z}\, d\tilde{x}\, d\tilde{y}\, d\tilde{z}$. Another related method (Smyth & Moum 2000*b*; Smyth *et al.* 2001), is to calculate $\widetilde{E}_p$ by "Thorpe reordering," (Thorpe 1977), in which the density is also adiabatically redistributed via sorting, but in this case the vertical distance, $\tilde{\eta}$, each fluid element traverses to obtain the lowest energy state is used to calculate the background potential energy, e.g.,$\widetilde{E}_b = \iiint \tilde{\rho}_t \tilde{g} \tilde{\eta}\, d\tilde{x}\, d\tilde{y}\, d\tilde{z}$. A third method of obtaining $\widetilde{E}_b$, suggested by Tseng & Ferziger (2001), involves taking the probability density function (PDF) of $\tilde{\rho}_t$, which can be thought of as a method of sorting the field into a minimum energy state. With the PDF of $\tilde{\rho}_t$, the vertical position of each parcel in a minimum energy state can be found, and then integrated over the vertical domain height to find $\widetilde{E}_b$.

The above methods for obtaining $\widetilde{E}_b$ rely on sorting methods. While avoiding the need for derivatives of density stratification, there are several drawbacks. First, as pointed out in Winters *et al.* (1995), sorting methods can only provide an estimate of background potential energy since the vertical position is discretized by the numerics, whereas in a physical system no such discretization exists. Second, since simulations are now becoming large (it is not uncommon for simulations to have on the order of one billion gridpoints), sorting or creating a PDF of a large field can take too long to be practical if values are to be obtained while the simulation is running. Lastly, to gain insight into Eulerian

energetics, it is desirable to calculate $\widetilde{E}_p$ locally, (i.e., at each grid point), whereas the above methods are only defined on a volume average basis.

Using a method that incorporates the work of Holliday & McIntyre (1981) and Winters *et al.* (1995) and the nondimensionalization specified in §2.2, the local E_p for a flow with a hyperbolic tangent background density profile is (see Appendix for full derivation):

$$E_p = \left(\frac{2\pi}{\overline{\mathrm{F}}_r}\right)^2 \left[(\rho_t)\mathrm{arctanh}\left(\frac{\varrho\rho}{\varrho^2 - \overline{\rho}\rho - \overline{\rho}^2}\right) + \frac{\varrho}{2}\ln\left(\frac{\varrho^2 - (\rho_t)^2}{\varrho^2 - \overline{\rho}^2}\right)\right], \tag{3.8}$$

where $\varrho = \Delta\rho/2$ is introduced simply for notational purposes. The time evolution of $\langle E_p \rangle$ for each ξ is shown in Figure 13(a), where the general trend is for $\langle E_p \rangle$ to be relatively independent of ξ until $\xi = 2$, after which there is a decrease in $\langle E_p \rangle$ with increasing ξ. This decrease in $\langle E_p \rangle$ can be explained by noting that by definition E_p is zero where there is no stratification since in the limit where $d\overline{\rho}(z)/dz \to 0$, $N \to 0$, and $\overline{\mathrm{F}}_r \to \infty$. Thus, when $\xi = 2$ the vertical span of E_p is narrower than the vertical span of w, which is a source term for E_p (see (A 14)). The volume averaged E_p will thus include the areas where E_p is zero. This can be seen in Figure 13(b), where the peak planar averaged $\langle E_p \rangle_H$ is nearly the same for all ξ even though there is a sharp the volume averaged $\langle E_p \rangle$ is sharply lower for high values of ξ than for low values.

3.2.3. *Mixing*

Mixing is an irreversible, small scale process affecting the thermodynamic state of a fluid. It is irreversible since the fluid can not be returned to its original, pre-mixed state. In contrast, stirring is a reversible, macroscopic process by which fluid elements move with respect to each other but remain unaffected (Peltier & Caulfield 2003). Mixing is typically quantified by the dissipation rates of kinetic and potential energy. The kinetic energy dissipate rate, ε, is the amount of kinetic energy that is dissipated into internal

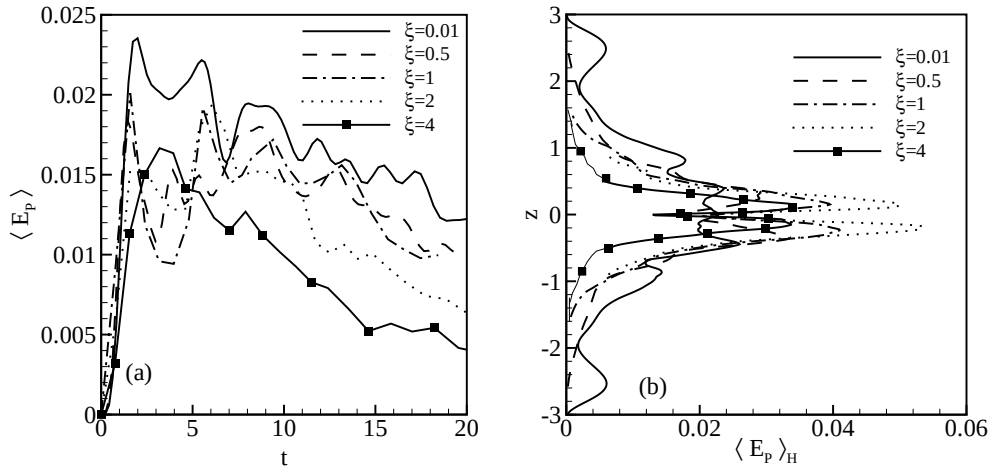

FIGURE 13. Evolution of (a) $\langle E_p \rangle$; (b) $\langle E_p \rangle_H$ at $t = 10$ for each ξ.

energy via viscous effects, and is defined as:

$$\varepsilon = \frac{2}{\mathrm{Re_r}} e_{ij} e_{ij} \,, \tag{3.9}$$

where e_{ij} is the strain rate tensor:

$$e_{ij} = \frac{1}{2}\left(\frac{\partial u_i}{\partial x_j} + \frac{\partial u_j}{\partial x_i}\right) \,. \tag{3.10}$$

The time evolution of the volume averaged kinetic energy dissipation rate $\langle \varepsilon \rangle$ for each simulation is shown in Figure 14. As the flows evolve, small scale turbulence forms and $\langle \varepsilon \rangle$ increases in time before decaying. There is a clear transition in the behavior of $\langle \varepsilon \rangle$ when $\xi = 4$. The reason for this transition can be explained by the behavior of $\left\langle S^2 \right\rangle_H$, the terms of which contribute to ε. When $\xi = 4$, $\left\langle S^2 \right\rangle_H$ is large outside the density stratification layer, which causes a significant amount of overturning and high $\langle \varepsilon \rangle$ early in the simulation (Figure 15).

The potential energy dissipation rate, χ, is the amount of available potential energy that is irreversibly dissipated to background potential energy. For the non-uniform density

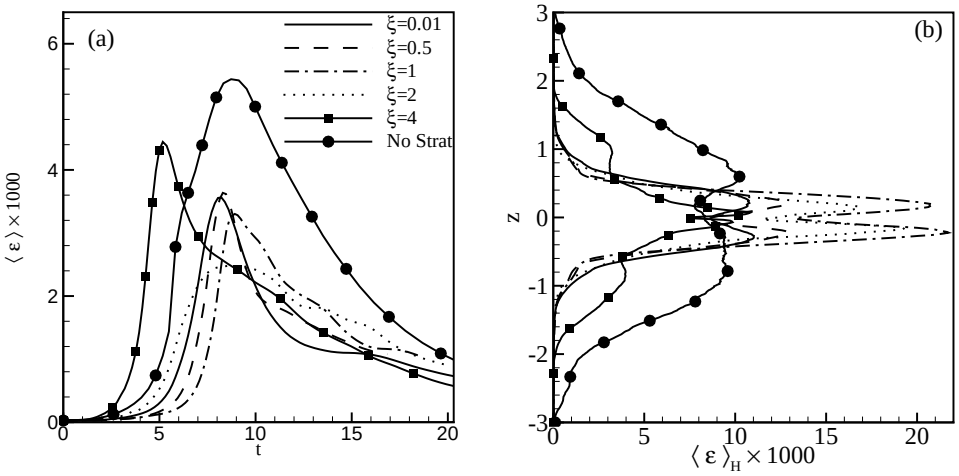

FIGURE 14. (a) Evolution of $\langle\varepsilon\rangle$ for each ξ; (b) $\langle\varepsilon\rangle_H$ at $t = 10$ for all ξ.

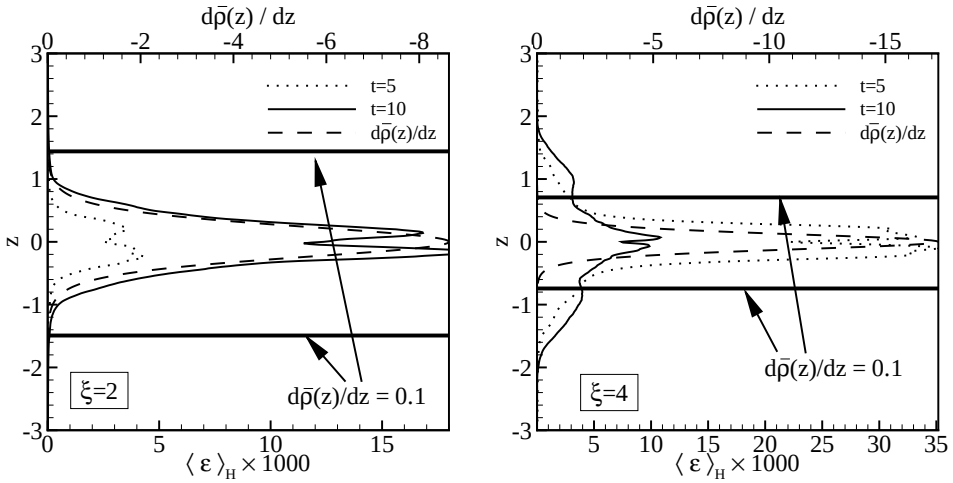

FIGURE 15. $\langle\varepsilon\rangle_H$ for (left) $\xi = 2$ and (right) $\xi = 4$ at $t = 5$ and 10. The dashed line represents the density stratification $d\overline{\rho}(z)/dz$. The bold solid lines identify where $|d\overline{\rho}(z)/dz| = 0.1$. (Note the difference in horizontal scales between plots.) When $\xi = 4$, much of the ε is formed earlier in time outside the stratification layer

stratification presented here, χ is defined as (see Appendix for derivation):

$$\chi = \frac{1}{\mathrm{Re_r Sc}} \left(\frac{2\pi}{\overline{\mathrm{F}}_r}\right)^2 \left[\mathrm{arctanh}\left(\frac{\varrho\rho}{\varrho^2 - \overline{\rho}\rho - \overline{\rho}^2}\right) \nabla^2\rho\right] . \tag{3.11}$$

The time evolution of $\langle\chi\rangle$ is shown in Figure 16(a). A transition in the behavior of $\langle\chi\rangle$

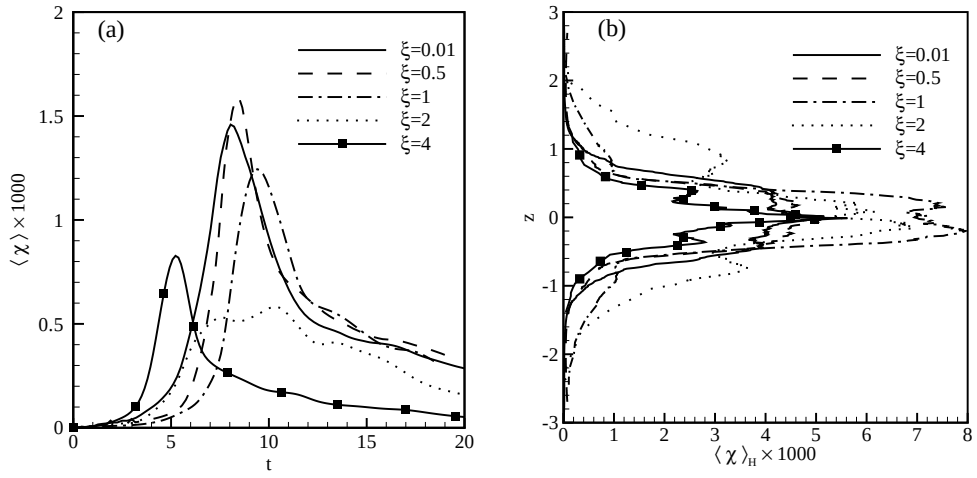

FIGURE 16. (a) Evolution of $\langle\chi\rangle$ for each ξ; (b) $\langle\chi\rangle_H$ for each ξ at $t = 10$

occurs between $\xi = 2$ and $\xi = 4$ with the maximum $\langle\chi\rangle$ occurring earlier and decaying more rapidly for the case with higher ξ. The early increase in magnitude in χ when $\xi = 4$ can be attributed to increased shear (and hence turbulent motions) caused by the intersection between the nearly unstratified and strongly stratified regimes. However, unlike ε, the magnitude of $\langle\chi\rangle$ decreases significantly in time when $\xi = 4$. The reason for the drop in magnitude is the same as for E_p; χ is zero by definition when there is no stratification.

The behavior of $\langle\varepsilon\rangle$ and $\langle\chi\rangle$ with respect to ξ has implication in modeling the Earth's energy budget. Ocean general circulation models (OGCM's) in which the density stratification is assumed to be linear show an imbalance in the Earth's energy budget by as much as 20% (Marmorino & Caldwell 1976; Robertson *et al.* 1995; Howard *et al.* 2004). This imbalance is consistent with assuming linear density stratification throughout the Earth's atmosphere and ocean instead of accounting for the non-uniform density gradients that have been observed. From Figures 14 and 16, one can see that for the same initial flow conditions, the peak $\langle\varepsilon\rangle$ is 25% higher when a sharp density gradient exists ($\xi = 4$) than when the flow is approximately linearly stratified ($\xi = 1$), while $\langle\chi\rangle$ is 50% lower.

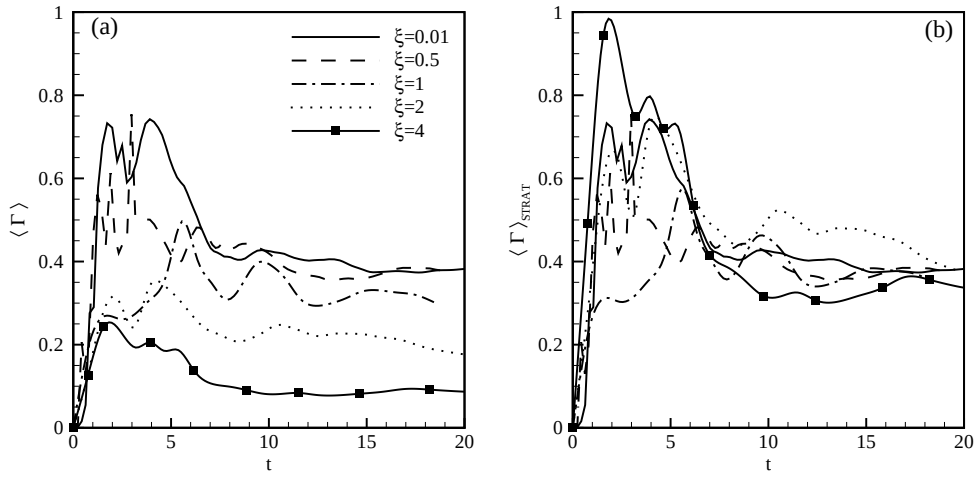

FIGURE 17. Evolution of (a) $\langle\Gamma\rangle$; (b) $\langle\Gamma\rangle_{STRAT}$, for each ξ.

These results suggest that assuming a uniform density gradient in areas of sharp density gradients leads to under-predicting mixing of kinetic energy ε, and over-predicting χ.

A related quantity of interest is the mixing efficiency, Γ, defined as the ratio of the rate at which potential energy is lost to background potential energy to the rate at which kinetic energy is lost to heat (Winters *et al.* 1995; Smyth *et al.* 2001):

$$\Gamma = \frac{\chi}{\varepsilon}\,. \tag{3.12}$$

Γ is of interest because in field experiments it is difficult to measure both ε and χ simultaneously due to the time scales required to measure each quantity (Gargett & Moum 1995). Thus, it would be convenient to measure one quantity and relate it to the other (Osborn 1980). The volume averaged mixing efficiency $\langle\Gamma\rangle = \langle\chi\rangle \,/\, \langle\varepsilon\rangle$ is shown in Figure 17(a), where the general trend is for a large initial $\langle\Gamma\rangle$ to occur up to $t \approx 7$, after which $\langle\Gamma\rangle$ settles to a constant value related to the value of ξ.

The rapid rise in $\langle\Gamma\rangle$ is clearly an artifact of the initial conditions of the simulations. Recall from Figure 10 that the simulations are initialized with no kinetic energy at small length scales and also that the initial available potential energy is zero. Small scales de-

velop more quickly in the density field than in the kinetic energy field, which results in increasing $\langle\Gamma\rangle$ at early time. Perhaps this characteristic of the flow is significant, but the initial conditions and the unity Schmidt number of the simulations must be accounted for when considering this result. As the flow develops and small-scale instabilities occur, ε increases and $\langle\Gamma\rangle$ decreases. These results are consistent with other numerical simulation results of uniformly stratified flows (e.g. Staquet 2000; Smyth *et al.* 2001; Riley & de Bruyn Kops 2003).

The vertical extent of the flow region subjected to significant stratification becomes smaller as ξ increases. This causes difficulty when interpreting volume averaged statistics of quantities that go to zero with decreasing stratification such as χ and Γ. In particular $\langle\chi\rangle$, and thus $\langle\Gamma\rangle$, will tend to be smaller for $\xi = 4$ than for $\xi = 1$ simply because of how the average is defined. It is of interest to know the mixing efficiency inside the density stratification layer (where $|d\overline{\rho}(z)/dz| > 0.1$, as defined above). Figure 17(b) contains a plot of the time evolution of $\langle\Gamma\rangle_{STRAT} = \langle\chi\rangle_{STRAT} \,/\, \langle\varepsilon\rangle_{STRAT}$, where $\langle\cdot\rangle_{STRAT}$ denotes average over the density stratification layer. As with $\langle\Gamma\rangle$, large initial values of $\langle\Gamma\rangle_{STRAT}$ can be seen. It is interesting to note that $\langle\Gamma\rangle_{STRAT}$ settles to near the same value for all ξ. This result suggests that in an area with non-uniform density stratification, the majority of mixing occurs in the region of high density gradient. This result is in agreement with the findings of St. Laurent & Schmitt (1999) and Schmitt (2003) in which increased mixing is found in the sharp density gradients of thermohaline staircases where salt fingering is prone to occur.

In stratified flows the importance of turbulence is often parameterized in terms of the buoyancy Reynolds number, $\mathrm{Re}_b = \widetilde{\varepsilon}/(\widetilde{\nu}\widetilde{\mathrm{N}}^2)$ (e.g. Gibson 1980; Imberger & Boashash 1986; Gregg 1987; Smyth & Moum 2000*b*). From this definition, $\mathrm{Re}_b = 21.5$ for one decade of turbulent length scales to form. Analysis by Gibson (1980) resulted in $\mathrm{Re}_b \approx 24$ for

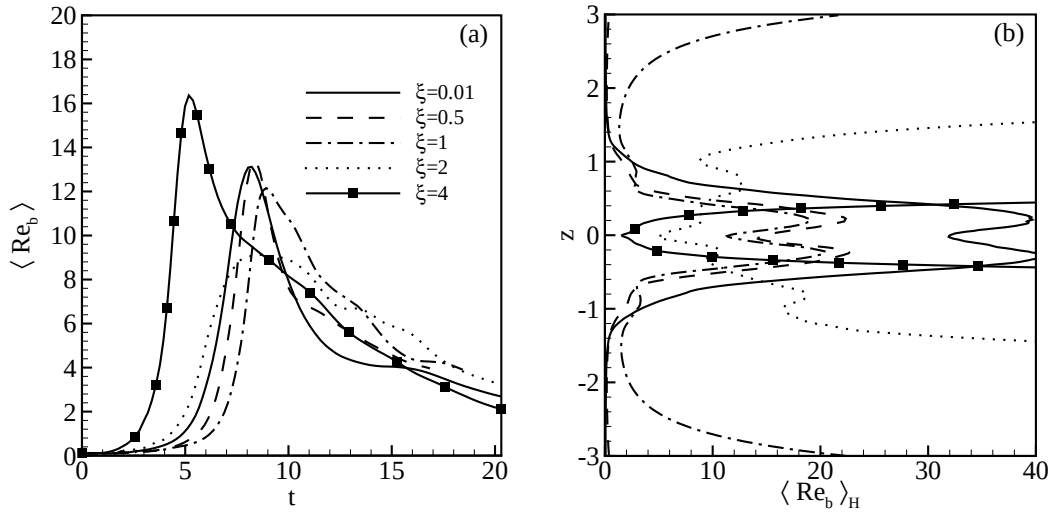

FIGURE 18. (a) Time evolution of $\langle \mathrm{Re}_b \rangle$ for each ξ; (b) $\langle \mathrm{Re}_b \rangle_H$ for each ξ at $t = 10$.

"active" turbulence to form. Since the local stratification varies with height, volume and planar averaged Re_b are defined here as:

$$\langle \mathrm{Re}_b \rangle = \frac{\langle \widetilde{\varepsilon} \rangle}{\widetilde{\nu}\widetilde{\overline{\mathrm{N}}}} \tag{3.13}$$

$$\langle \mathrm{Re}_b \rangle_H = \frac{\langle \widetilde{\varepsilon} \rangle_H}{\widetilde{\nu}\widetilde{\mathrm{N}}(\tilde{z})} \tag{3.14}$$

where $\widetilde{\mathrm{N}}^2(\tilde{z}) = \tilde{g}/\tilde{\rho}_0 d\tilde{\overline{\rho}}(\tilde{z})/d\tilde{z}$ is the buoyancy frequency at vertical position $\tilde{z}$, and $\widetilde{\overline{\mathrm{N}}}$ is defined above. The time evolution of $\langle \mathrm{Re}_b \rangle$ is shown in Figure 18(a), where the peak $\langle \mathrm{Re}_b \rangle$ is between 12 and 16 which suggests that the flow does not have an adequate range of length scales for turbulence to form. However, one must consider that volume averages incorporate areas of small Re_b near the wake edge. In Figure 18(b) the peak planar averaged buoyancy Reynolds number is shown to be between 18 and 40. Note that away from the centerline, the energy in the flow approaches zero and turbulence is not expected. However, $\widetilde{\mathrm{N}}(\tilde{z})$ also approaches zero away from the centerline, which results in high $\langle \mathrm{Re}_b \rangle_h$. Also, the effect of the local stratification is evident as $\langle \mathrm{Re}_b \rangle_H$ decreases sharply between $\xi = 0.01$ and 0.5.

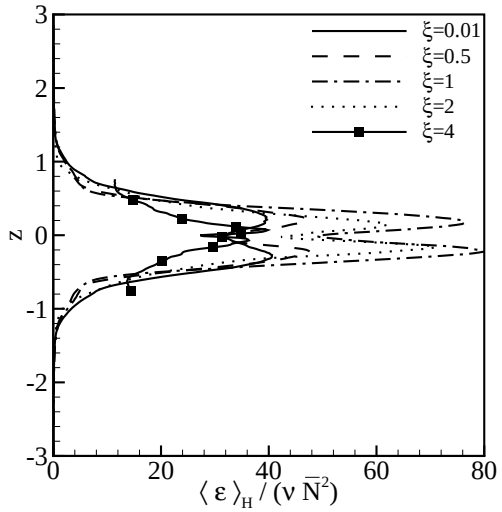

FIGURE 19. Buoyancy Reynolds number defined in terms of the average buoyancy frequency $\langle\widetilde{\varepsilon}\rangle_H/(\tilde{\nu}\widetilde{\overline{\mathrm{N}}})$.

An interesting question that arises is what would the planar averaged Re_b be if the average density stratification, $\Delta\overline{\rho}/\Delta z$, is assumed? With this assumption, the planar averaged buoyancy Reynolds number is defined as $\langle\widetilde{\varepsilon}\rangle_H/(\tilde{\nu}\widetilde{\overline{\mathrm{N}}})$, and is shown in Figure 19. The effect of assuming $\Delta\overline{\rho}/\Delta z$ would result in Re_b being over estimated by as much as 8 times for a sharp density gradient ($\xi = 4$) case, which could result in incorrect turbulence parameterization based on Re_b.

In field studies $\widetilde{\varepsilon}$ is usually inferred from measurements of one or two components of the strain rate tensor. In strong, stable density stratification it is often assumed that vertical shear causes most of $\widetilde{\varepsilon}$, leading to the relation

$$\tilde{\nu}\widetilde{S}^2 \approx \widetilde{\varepsilon}. \tag{3.15}$$

This relationship has been shown to hold for a large range of Reynolds numbers, and it has been shown that the ratio $\tilde{\nu}\widetilde{S}^2/\widetilde{\varepsilon} \approx 0.9$ (Fincham *et al.* 1996; Praud *et al.* 2005). Hebert & de Bruyn Kops (2006*b*) show that (3.15) is valid only when the buoyancy Reynolds number $\mathrm{Re}_b < \mathcal{O}(1)$. Figure 20 contains a plot of the ratio $\tilde{\nu}\left\langle\widetilde{S}^2\right\rangle/\langle\widetilde{\varepsilon}\rangle$ versus

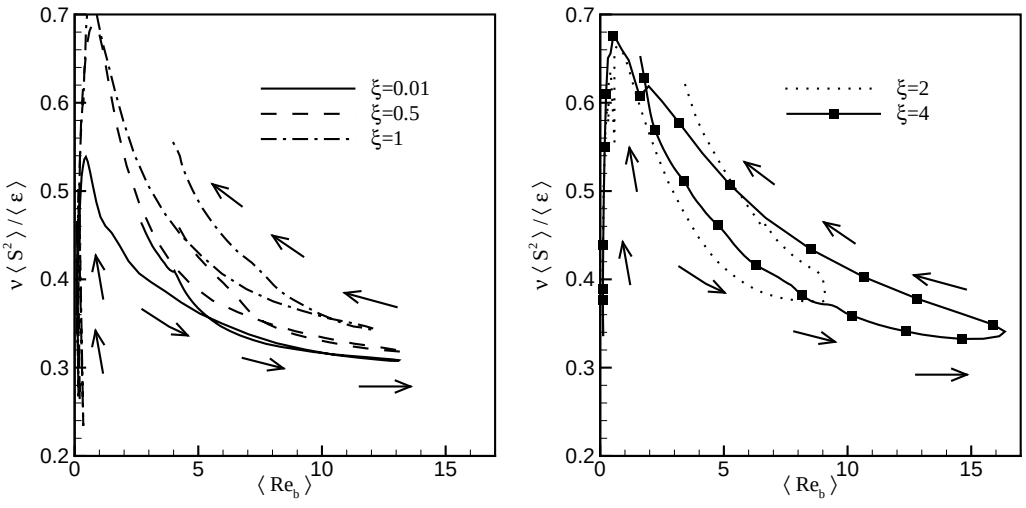

FIGURE 20. $\tilde{\nu}\left\langle \widetilde{S}^2 \right\rangle / \langle \widetilde{\varepsilon} \rangle$ versus $\langle \mathrm{Re}_b \rangle$ for each ξ. Arrows denote direction of increasing time.

Re_b for each of the simulated flows in this study. As the flow develops and turbulence forms, $\nu \langle S^2 \rangle / \langle \varepsilon \rangle$ decreases to below 0.5, while $\langle \mathrm{Re}_b \rangle$ increases above 1. Then, as the flow decays, $\langle \mathrm{Re}_b \rangle$ decreases back to below 1, and the ratio $\tilde{\nu}\left\langle \widetilde{S}^2 \right\rangle / \langle \widetilde{\varepsilon} \rangle$ approaches 0.8, in agreement with the aforementioned studies.

In order to see if (3.15) holds locally, the quantity $\tilde{\nu}\left\langle \widetilde{S}^2 \right\rangle_H / \langle \widetilde{\varepsilon} \rangle_H$ is shown in Figure 21. In comparing with Figure 18(b), one can see that locally $\tilde{\nu}\left\langle \widetilde{S}^2 \right\rangle_H / \langle \widetilde{\varepsilon} \rangle_H \approx 0.8$ only for $\xi = 4$, where $\langle \mathrm{Re}_b \rangle_H < 1$.

4. Modeling Implications and Conclusions

Simulation results are presented for flows initialized with a von Kármán vortex street and no mean velocity or shear, similar to a momentumless wake. Each simulation is subject to non-uniform density stratification to represent a wake in natural settings such as that found in an atmospheric transition layer or thermohaline staircase. The average stratification for all the cases is the same so the only simulation parameter that is adjusted is ξ, the ratio of the wake height to the stratification profile height. The

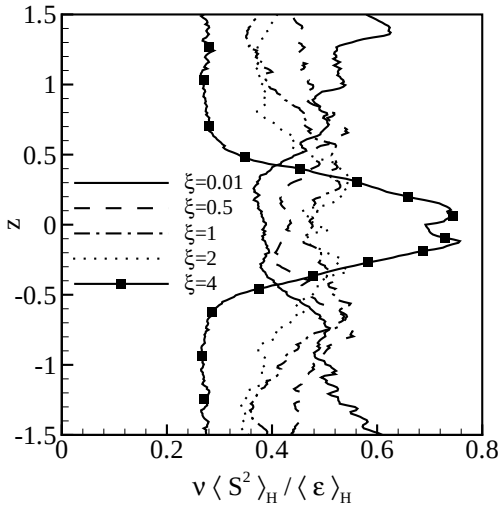

FIGURE 21. $\tilde{\nu}\left\langle \widetilde{S}^2 \right\rangle_H / \langle \widetilde{\varepsilon} \rangle_H$ for each ξ at $t = 10$.

average stratification is strong enough so that the average Froude number is order one. Comparisons to the unstratified case are also made since it is observed that flows in which the density changes over a very short vertical range have certain characteristics more like those of unstratified than stratified flows. Additionally, an analytical expression for the local available potential energy assuming a steady $\mathrm{sech}^2(z)$ vertical stratification profile flow is derived, which enables local analysis of flow energetics.

The simulated flows in which the wake height is less than or equal to twice the density layer height ($\xi \leq 2$) are observed to be consistent with the current understanding of strongly stratified flow, in particular, increasing horizontal and decreasing vertical length scales as the flows evolve. These characteristics are in agreement with the scaling arguments of Riley *et al.* (1981) and the horizontal layer decoupling heuristic by Lilly (1983). When the wake height is greater that twice the density layer height ($\xi > 2$), however, the importance of the density stratification is diminished and the flows demonstrate characteristics of non-stratified flows. In particular, $\langle E_H \rangle$ dissipates faster, and $\langle E_V \rangle$, $\langle \varepsilon \rangle$, and $\langle \chi \rangle$ increase much faster and to much higher values than in the cases with $\xi \leq 2$.

The transition point of $\xi \approx 2$ suggests that it is the relation between the stratification profile and the energy profile, rather than the velocity profile, that determines if the flow will behave primarily as stratified or unstratified in terms of global statistics. Rather than simply concluding that the observed results might be explained by energetics, it worthwhile to briefly consider instability mechanisms. The Kelvin-Helmholtz (KH) instability is typically assumed to be the dominant instability mechanism in stratified flows. In shear flows where the density length scale becomes smaller than the velocity length scale, however, theoretical analysis first performed by Holmboe (1962) showed an oscillatory instability. Evidence of the Holmboe instability has been observed in the atmosphere (e.g., Emmanuel *et al.* 1972) and ocean (e.g., Yonemitsu *et al.* 1996). Transition from KH to Holmboe instability has been investigated theoretically (e.g., Smyth & Peltier 1989; Ortiz *et al.* 2002), experimentally (e.g., Zhu & Lawrence 2001; Hogg & Ivey 2003) and numerically (e.g., Hazel 1972; Smyth *et al.* 1988). In particular, Smyth & Winters (2003) demonstrate that when the ratio of velocity to density length scales is greater than 2.4 then Holmboe instability becomes dominant. A significant difference between those experiments and ours is that our simulations have no mean shear. Also, we are considering the wake of an object rather than a shear plane. Nevertheless, the results of Smyth & Winters (2003) support our conclusion that stratified flow configurations with the equivalent of $\xi > 2$ should not be expected to behave like uniformly stratified flows.

One motivation for studying flows subject to non-linear stratification is to improve ocean and atmospheric modeling. The results of this study suggest that modeling a sharp localized density gradient with a uniform density profile having the same average density gradient will result in underpredicting $\langle\varepsilon\rangle$ up to 25% and overpredicting $\langle\chi\rangle$ by as

much as 50%. This result is consistent with the trends in the errors in the global energy budget predicted by general circulation models.

Finally, the volume-averaged mixing efficiency, $\langle\Gamma\rangle$, is observed to be significantly lower when $\xi > 2$ than for $\xi < 2$. This difference in $\langle\Gamma\rangle$ is a result of χ approaching zero when there is no stratification. In contrast, the mixing efficiency averaged over only the region with significant stratification is between 0.3 and 0.5 for all simulations, which is in agreement with measurements and simulations in uniformly stratified flows.

The authors thank Jim Riley and Kraig Winters for the concept of vortex street simulations, and Kaustubh Rao for his comments on the derivation in the appendix. This research is funded by the U.S. Office of Naval Research, Grant No. N00014-04-1-0687 managed by Dr. R. D. Joslin. Grants of high performance computer time were provided by the Arctic Region Supercomputing Center and the Army Engineer Research and Development Center.

REFERENCES

Beckers, M., Clerx, H. J. H., van Heijst, G. J. F. & Verzicco, R. 2002 Dipole formation by two interacting shielded monopoles in a stratified fluid. *Phys. Fluids* **14**, 704.

Beckers, M., Verzicco, R., Clercx, H. J. H. & van Heijst, G. J. F. 2001 Dynamics of pancake-like vortices in a stratified fluid: experiments, model and numerical simulations. *J. Fluid Mech.* **433**, 1–27.

Billant, P. & Chomaz, J. M. 2000*a* Experimental evidence for a new instability of a vertical columnar vortex pair in a strongly stratified fluid. *J. Fluid Mech.* **418**, 167–188.

Billant, P. & Chomaz, J. M. 2000*b* Theoretical analysis of the zigzag instability of a vertical columnar vortex pair in a strongly stratified fluid. *J. Fluid Mech.* **419**, 29–63.

Billant, P. & Chomaz, J. M. 2000*c* Three-dimensional stability of a vertical columnar vortex pair in a stratified fluid. *J. Fluid Mech.* **419**, 65–91.

Billant, P. & Chomaz, J. M. 2001 Self-similarity of strongly stratified inviscid flows. *Phys. Fluids* **13**, 1645–1651.

Bonnier, M. & Eiff, O. 2002 Experimental investigation of the collapse of a turbulent wake in a stably stratified fluid. *Phys. Fluids* **14**, 791.

Boyd, J. D. 1989 Properties of thermal staircase off the northeast coast of South America. *J. Geophys. Res.* **94**, 8303–8312.

Boyd, J. P. 2001 *Chebyshev and Fourier Spectral Methods*. Dover.

de Bruyn Kops, S. M., Riley, J. J. & Winters, K. B. 2003 Reynolds and Froude number scaling in stably-stratified flows. In *Reynolds Number Scaling in Turbulent Flow*. Kluwer.

Chomaz, J.-M., Bonneton, P., Butet, A. & Hopfinger, E. J. 1993 Vertical diffusion of the far wake of a sphere moving in a stratified fluid. *Phys. Fluids A* **5**, 2799.

Dalaudier, F., Sidi, C., Crochet, M. & Vernin, J. 1994 Direct evidence of "sheets" in the atmospheric temperature field. *J. Atmos. Sci.* **51**, 237–248.

D'Asaro, E. A., Winters, K. B. & Lien, R. C. 2004 Lagrangian estimates of diapycnal mixing in a simulated K-H instability. *J. Atmos. Oceanic Technol.* **21**, 799–809.

Emmanuel, C. B., Bean, B., McAllister, R. & Pollard, J. R. 1972 Observations of

Helmholtz waves in the lower atmosphere with an accoustic sounder. *J. Atmos. Sci.* **29**, 886–892.

Fincham, A. M., Maxworthy, T. & Spedding, G. R. 1996 Energy dissipation and vortex structure in freely decaying, stratified grid turbulence. *Dyn. Atmos. Oceans* **23**, 155–169.

Gargett, A. E., Merryfield, W. J. & Holloway, G. 2003 Direct numerical simulation of differential scalar diffusion in three-dimensional stratified turbulence. *J. Phys. Oceanogr.* **33**, 1758–1782.

Gargett, A. E. & Moum, J. N. 1995 Mixing efficiencies in turbulent tidal fronts - results from direct and indirect measurements of density flux. *J. Phys. Oceanogr.* **25**, 2583–2608.

Gibson, C. H. 1980 Fossil turbulence, salinity, and vorticity turbulence in the ocean. In *Marine Turbulence* (ed. J. C. Nihous), pp. 221–257. Elsevier.

Gill, E. 1982 *Atmossphere-Ocean Dynamics*. Academic Press.

Gossard, E. E., Gaynor, J. E., Zamora, R. J. & Neff, W. D. 1985 Finestructure of elevated stable layers observed by sounder and in situ tower sensors. *J. Atmos. Sci.* **4**, 113–131.

Gregg, M. C. 1987 Diapycnal mixing in the thermocline – a review. *J. Geophys. Res.–Oceans* **92**, 5249–5286.

Gregg, M. C. & Sanford, T. 1987 Shear and turbulence in a thermohaline staircase. *Deep-Sea Research* **34**, 1689–1696.

Hazel, P. 1972 Numerical studies of the stability of inviscid parallel shear flows. *J. Fluid Mech.* **51**, 39–62.

Hebert, D. A. & de Bruyn Kops, S. M. 2006*a* Predicting turbulence in flows with strong stable stratification. *Phys. Fluids* **18** (6), 1–10.

Hebert, D. A. & de Bruyn Kops, S. M. 2006*b* Relationship between vertical shear rate and kinetic energy dissipation rate in stably stratified flows. *Geophys. Res. Let.* **33**, L06602, doi:10.1029/2005GL025071.

Herring, J. R. & Métais, O. 1989 Numerical experiments in forced stably stratified turbulence. *J. Fluid Mech.* **202**, 97.

Hogg, A. M. & Ivey, G. N. 2003 The Kelvin-Helmholtz to Holmboe instability transition in stratified exchange flows. *J. Fluid Mech.* **477**, 339–362.

Holliday, D. & McIntyre, M. 1981 On potential energy density in an incompressible, stratified fluid. *J. Fluid Mech.* **107**, 221–225.

Holmboe, J. 1962 On the behavior of symmetric waves in stratified shear layers. *Geophys. Publ.* **24**, 67–113.

Howard, S. L., Hyatt, J. & Padman, L. 2004 Mixing in the pycnocline over the western Antarctic Peninsula shelf during Southern Ocean GLOBEC. *Deep Sea Research II* **51**, 1965–1979.

Imberger, J. & Boashash, B. 1986 Application of the Winger-Ville distribution to temperature gradient microstructure: A new technique to study small-scale variations. *J. Phys. Oceanogr.* **16**, 1997–2012.

Ivey, G. N. & Imberger, J. 1991 On the nature of turbulence in a stratified fluid. part 1: The energetics of mixing. *J. Phys. Oceanogr.* **21**, 650–658.

Jacobitz, F. G., Sarkar, S. & VanAtta, C. W. 1997 Direct numerical simulations of the turbulence evolution in a uniformly sheared and stably stratified flow. *J. Fluid Mech.* **342**, 231–261.

Kerr, R. M. 1985 Higher-order derivative correlations and the alignment of small-scale structures in isotropic turbulence. *J. Fluid Mech.* **153** (31), 31.

Kolmogorov, A. N. 1962 A refinement of previous hypotheses concerning the local structure of turbulence in a viscous incompressible fluid at high Reynolds number. *J. Fluid Mech.* **13**, 82–85.

Lambert, R. B. & Sturges, W. 1977 A thermohaline staircase and vertical mixing in the thermocline. *Deep-Sea Research* **24**, 211–222.

Lilly, D. K. 1983 Stratified turbulence and the mesoscale variability of the atmosphere. *J. Atmos. Sci.* **40**, 749–761.

Lindborg, E. 2006 The energy cascade in a strongly stratified fluid. *J. Fluid Mech.* **550**, 207–242.

Liu, H. T. 1995 Energetics of grid turbulence in a stably stratified fluid. *J. Fluid Mech.* **296**, 127–157.

Lorenz, E. N. 1955 Available potential energy and the maintenance of the general circulation. *Tellus* **7**, 157–167.

Marmorino, G. O. & Caldwell, D. R. 1976 Heat and salt transport through a diffusive thermohaline interface. *Deep Sea Research* **23**, 59–67.

Métais, O. & Herring, J. R. 1989 Numerical simulations of freely evolving turbulence in stably stratified fluids. *J. Fluid Mech.* **202**, 117.

Meunier, P. & Spedding, G. 2006 Stratified propelled wakes. *J. Fluid Mech.* **522**, 229–256.

Moin, P. & Mahesh, K. 1998 Direct numerical simulation: A tool in turbulence research. *Annu. Rev. Fluid Mech.* **30**, 539–578.

Molcard, R. & Tait, R. I. 1977 The steady state of the step structure in the Tyrrhenian Sea. In *A voyage of discovery* (ed. M. V. Angel), pp. 221–233. New York:Pergamon Press.

Muschinski, A. & Wode, C. 1998 First in situ evidence for coexisting submeter temperature and humidity sheets in the lower free troposphere. *J. Atmos. Sci.* **55** (18), 2893–2905.

Ortiz, S., Chomaz, J. M. & Loiseleux, T. 2002 Spatial Holmboe instability. *Phys. Fluids* **14** (8), 2585–2597.

Osborn, T. R. 1980 Estimates of the local-rate of vertical diffusion from dissipation measurements. *J. Phys. Oceanogr.* **10**, 83–89.

Peltier, W. R. & Caulfield, C. P. 2003 Mixing efficiency in stratified shear flows. *Annu. Rev. Fluid Mech.* **35**, 135–167.

Praud, O., Fincham, A. M. & Sommeria, J. 2005 Decaying grid turbulence in a strongly stratified fluid. *J. Fluid Mech.* **522**, 1–33.

Riley, J. J. & de Bruyn Kops, S. M. 2003 Dynamics of turbulence strongly influenced by buoyancy. *Phys. Fluids* **15** (7), 2047–2059.

Riley, J. J. & Lelong, M. P. 2000 Fluid motions in the presence of strong stable stratification. *Annu. Rev. Fluid Mech.* **32**, 613–657.

Riley, J. J., Metcalfe, R. W. & Weissman, M. A. 1981 Direct numerical simulations of homogeneous turbulence in density stratified flows. In *Proc. AIP Conf. Nonlinear Properties of Internal Waves* (ed. B. J. West), pp. 79–112. New York: American Institute of Physics.

Robertson, R., Padman, L. & Levine, M. D. 1995 Finestructure, microstructure, and vertical mixing processes in the upper ocean in the western wedell sea. *JGR* **100**, 18517–18536.

Schmitt, R. W. 2003 Observational and laboratory insights into salt finger convection. *Progress in Oceanography* **56**, 419–433.

Schmitt, R. W., Perkins, H., Boyd, J. D. & Stalcup, M. C. 1987 C-SALT: An investigation of the thermohaline staircase in the western tropical North Atlantic. *Deep-Sea Research* **34**, 1655–1665.

Shih, L. H., Koseff, J. R., Ivey, G. N. & Ferziger, J. H. 2005 Parameterization of turbulent fluxes and scales using homogeneous sheared stably stratified turbulence simulations. *J. Fluid Mech.* **525**, 193–214.

Smyth, W. D., Klaassen, G. P. & Peltier, W. R. 1988 Finite-amplitude holmboe waves. *Geophys. Astrophys. Fluid Dyn.* **43**, 181–222.

Smyth, W. D. & Moum, J. N. 2000*a* Anisotropy of turbulence in stably stratified mixing layers. *Phys. Fluids* **12**, 1343–1362.

Smyth, W. D. & Moum, J. N. 2000*b* Length scales of turbulence in stably stratified mixing layers. *Phys. Fluids* **12**, 1327–1342.

Smyth, W. D., Moum, J. N. & Caldwell, D. R. 2001 The efficiency of mixing in turbulent patches: inferences from direct simulations and microstructure observations. *J. Phys. Oceanogr.* **31**, 1969–1992.

Smyth, W. D., Nash, J. D. & Moum, J. N. 2005 Differential diffusion in breaking Kelvin-Helmholtz billows. *J. Phys. Oceanogr.* **35**, 1004–1022.

Smyth, W. D. & Peltier, W. R. 1989 The transition between kelvin-helmholtz and holmboe instability - an investigation of the overreflection hypothesis. *J. Atmos. Sci.* **46**, 3698–3720.

Smyth, W. D. & Winters, K. B. 2003 Turbulence and mixing in Holmboe waves. *J. Phys. Oceanogr.* **33**, 694–711.

Spedding, G. R. 2002 Vertical structure in stratified wakes at high initial froude number. *J. Fluid Mech.* **454**, 71.

Spedding, G. R., Browand, F. K. & Fincham, A. M. 1996 Turbulence, similarity scaling

and vortex geometry in the wake of a towed sphere in a stably stratified fluid. *J. Fluid Mech.* **314**, 53.

Spiegel, E. A. & Veronis, G. 1960 On the Boussinesq approximation for a compressible fluid. *Astrophys J.* **131**, 442–447.

St. Laurent, L. & Schmitt, R. W. 1999 The contribution of salt fingers to vertical mixing in the North Atlantic tracer release experiment. *J. Phys. Oceanogr.* **29**, 1404–1424.

Staquet, C. 2000 Mixing in a stably-stratified shear layer: two- and three-dimensional numerical experiments. *Fl. Dyn. Res.* **27**, 367.

Thorpe, S. A. 1977 Turbulence and mixing in a Scottish loch. *Philos. Trans. Roy. Soc. London* **A286**, 125–181.

Tseng, Y.-h. & Ferziger, J. H. 2001 Mixing and available potential energy in stratified flows. *Phys. Fluids* **13** (5), 1281–1293.

Waite, M. & Bartello, P. 2004 Stratified turbulence dominated by vortical motion. *J. Fluid Mech.* **517**, 281–308.

Williams, A. J. 1974 Salt fingers observed in the Mediterranean outflow. *Science* **185**, 941–943.

Winters, K. B. & D'Asaro, E. A. 1996 Diascalar flux and the rate of fluid mixing. *J. Fluid Mech.* **317**, 179–193.

Winters, K. B., Lombard, P. N., Riley, J. J. & D'Asaro, E. A. 1995 Available potential energy and mixing in density-stratified fluids. *J. Fluid Mech.* **289**, 115–128.

Yonemitsu, N., Swaters, G., Rajaratnam, N. & Lawrence, G. 1996 Shear instabilities in arrested salt-wedge flows. *Dyn. Atmos. Oceans* **24**, 173–182.

Zhu, D. & Lawrence, G. 2001 Holmboe's instability in exchange flows. *J. Fluid Mech.* **429**, 391–409.

Appendix. Available potential energy for non-uniform stratification

Available potential energy for uniformly stratified flow is usually defined locally as (e.g. Gill 1982, p.140):

$$E_p = -\frac{1}{2}\frac{g}{\rho_0}\frac{1}{d\overline{\rho}/dz}\rho^2\,, \tag{A 1}$$

where $\rho(x,y,z,t)$ is the fluctuation from the undisturbed density $\overline{\rho}$, and $d\overline{\rho}/dz$ is constant in space and time. Note that in this appendix, all quantities are dimensional but the $(\bar{\cdot})$ notation has been dropped for convenience. When density stratification is non-uniform, the definition of potential energy is more complicated because the derivative of the stratification, $d^2\overline{\rho}(z)/dz^2 \neq 0$, is not zero (Holliday & McIntyre 1981).

A method to obtain an exact expression for potential energy in an incompressible fluid with non-uniform density stratification is put forth by Holliday & McIntyre (1981). In that derivation, it is assumed that the flow is inviscid. Here we do not rule out diffusive effects but assume, as we have throughout this paper, that the background stratification is constant such as in a persistent, steady-state thermohaline staircase or atmospheric transition layer. We begin with the definition of the available potential energy of a fluid element located at $\vec{x} = (x,y,z)$ (Winters *et al.* 1995),

$$E_p = g\rho_t(\vec{x},t)(z - z^*)\ , \tag{A 2}$$

where z^* is the vertical coordinate of the fluid element when the field has been sorted to have the lowest possible potential energy.

The material derivative of E_p is

$$\frac{DE_p}{Dt} = g\frac{D}{Dt}\left[\rho_t\left(\vec{x},t\right)\left(z - z^*\right)\right]\ . \tag{A 3}$$

Noting that $\rho_t\left(\vec{x},t\right) = \overline{\rho}\left(z\right) + \rho\left(\vec{x},t\right)$, that for a fluid element with $\rho = \overline{\rho}$, $z = z^*$, and

adopting the notion $\zeta = z - z^*$, A 3 can be written as

$$\frac{DE_p}{Dt} = \frac{D}{Dt}\left\{g\rho\left(\vec{x},t\right)\zeta\right\} \tag{A 4}$$

$$= \frac{D}{Dt}\left\{g\left[\overline{\rho}\left(z-\zeta\right)-\overline{\rho}(z)\right]\zeta\right\} \ . \tag{A 5}$$

Recalling that $\overline{\rho}$ is steady and $\frac{D}{Dt}\left(\zeta\right) = w$, i.e. the vertical velocity of the fluid element,

$$\frac{DE_p}{Dt} = gw\left[\overline{\rho}\left(z-\zeta\right)-\overline{\rho}(z)\right] \ . \tag{A 6}$$

From this point, the derivation follows that of Holliday & McIntyre (1981).

Because our numerical simulations involve a field of density fluctuations, $\rho(x,y,z,t)$, it is advantageous to write E_p in terms of $\overline{\rho}(z)$ and $\rho(x,y,z,t)$ rather than z, ζ, which is possible because $\rho(x,y,z,t)$ contains Lagrangian information required to compute (A 6). Converting to $\overline{\rho}(z)$ and $\rho(x,y,z,t)$ can be achieved by first defining a potential function $\Phi\{\}$ as:

$$\Phi\{\overline{\rho}(z)\} = gz. \tag{A 7}$$

Provided the undisturbed stratification $\overline{\rho}(z)$ is stable everywhere, (A 6) can be written in the following form (Holliday & McIntyre 1981):

$$E_p = -\int_0^{\rho}\left[\Phi\{\overline{\rho}(z)+\rho'\}-\Phi\{\overline{\rho}(z)\}\right]d\rho', \tag{A 8}$$

where again prime denotes a dummy integration variable, and the spatial dependence (x,y,z,t) of ρ is implied. For the specific hyperbolic tangent $\overline{\rho}(z)$ given in (2.2), (A 7) can be shown to be

$$\Phi\{\overline{\rho}(z)\} = -g\delta_\rho \operatorname{arctanh}\left(\frac{\overline{\rho}(z)}{\varrho}\right), \tag{A 9}$$

which, after substituting into (A 8), yields the following expression for E_p (where the z dependence of $\overline{\rho}$ is implied, and the expression is divided by a reference density ρ_0 to make E_p per unit mass):

$$E_p = \frac{g\delta_\rho}{\rho_0}\left[(\overline{\rho}+\rho)\operatorname{arctanh}\left(\frac{\varrho\rho}{\varrho^2-\overline{\rho}\rho-\overline{\rho}^2}\right)+\frac{\varrho}{2}\ln\left(\frac{\varrho^2-(\overline{\rho}+\rho)^2}{\varrho^2-\overline{\rho}^2}\right)\right] \tag{A 10}$$

An interesting question that arises is how does this differ from the potential energy of (A 1). This can be seen by taking a Taylor series of (A 10) about $\rho = 0$. With some algebraic manipulation, the first 3 terms of the Taylor series can be shown to be:

$$E_p \approx -\frac{1}{2}\frac{g}{\rho_0}\frac{1}{d\overline{\rho}(z)/d(z)}\rho^2 - \frac{1}{3}\frac{g}{\rho_0}\frac{\overline{\rho}(z)}{\delta_\rho \varrho (d\overline{\rho}(z)/d(z))^2}\rho^3 - \frac{1}{12}\frac{g}{\rho_0}\frac{\varrho + 3\overline{\rho}(z)}{\varrho\delta_\rho^2 (d\overline{\rho}(z)/d(z))^3}\rho^4 \quad \text{(A 11)}$$

In the limit of linearized motion (which is typically how (A 1) is derived), terms of order greater than ρ^2 are assumed small and neglected. Thus, neglecting higher order terms in (A 10) results in (A 1).

The time derivative of E_p can be found by use of the chain rule:

$$\frac{\partial E_p}{\partial t} = \frac{\partial E_p}{\partial \rho}\frac{\partial \rho}{\partial t}. \quad \text{(A 12)}$$

Note the term $\partial E_p/\partial\rho$ is the inverse of the integral (A 8). Thus, for the hyperbolic tangent stratification studied here, $\partial E_p/\partial t$ becomes

$$\frac{\partial E_p}{\partial t} = \frac{g\delta_\rho}{\rho_0}\text{arctanh}\left(\frac{\varrho\rho}{\varrho^2 - \overline{\rho}\rho - \overline{\rho}^2}\right)\frac{\partial \rho}{\partial t}. \quad \text{(A 13)}$$

which, when substituting the dimensional form of $(2.5c)$ for $\partial\rho/\partial t$, becomes:

$$\frac{\partial E_p}{\partial t} = -T_p + B - \chi \quad \text{(A 14)}$$

where T_p is a transport term, B is buoyancy flux, and χ is the rate of conversion from available to background potential energy:

$$\begin{aligned} T_p &= -g\delta_\rho\left[\text{arctanh}\left(\frac{\varrho\rho}{\varrho^2 - \overline{\rho}\rho - \overline{\rho}^2}\right)\mathbf{v}\cdot\nabla\rho\right] \\ B &= -g\delta_\rho\left[\text{arctanh}\left(\frac{\varrho\rho}{\varrho^2 - \overline{\rho}\rho - \overline{\rho}^2}\right)w\frac{d\overline{\rho}(z)}{dz}\right] \\ \chi &= -g\delta_\rho D\left[\text{arctanh}\left(\frac{\varrho\rho}{\varrho^2 - \overline{\rho}\rho - \overline{\rho}^2}\right)\nabla^2\rho\right] \end{aligned}$$